



Adaptive Multi-objective Sliding Mode Control of a Wind Energy Conversion System Involving Doubly Fed Induction Generator for Power Capture Optimization

Karim Noussi¹  · Abdelmajid Abouloifa² · Fouad Giri³ · Hanane Katir¹ · Ibtissam Lachkar² · Meriem Aourir¹ · Chaouqi Aouadi¹ · Josep M. Guerrero⁴

Received: 5 December 2020 / Revised: 23 June 2021 / Accepted: 2 August 2021 / Published online: 3 September 2021

© Brazilian Society for Automatics–SBA 2021

Abstract

We consider the problem of controlling wind energy conversion systems that are based on doubly fed induction generators. The aim is to design a nonlinear controller to fulfill the control goals considering the two sides, grid and rotor side. On the rotor side, the control objectives are twofold: (i) ensuring the maximum power point tracking requirement and (ii) maintaining the stator reactive power at a desired reference. On the grid side, we also seek the achievement of two control objectives: (i) regulating the DC-link voltage at a given reference value and (ii) ensuring a zero reactive power. Besides the multi-objective nature of this study, the difficulty of the control problem lies in the nonlinearity and uncertainty of the system dynamics and external disturbances. The control problem under consideration is dealt with by designing a model-based controller using the adaptive sliding mode technique. The stability and performances of the closed-loop control system are analyzed both theoretically and by numerical simulations. The latter are performed using 2MW grid-connected wind turbine system in MATLAB/SIMULINK/SimPowerSystems environment. The simulation results confirm that the suggested controller meets its objectives and features robustness properties.

Keywords Adaptive SMC · DFIG · Lyapunov stability · Powers control · Wind energy conversion system (WECS)

1 Introduction

In recent years, renewable energy based on wind and solar resources stood as the main alternative to fossil fuel, especially for electricity production (Şeker et al. 2016; Katir et al. 2020). As a matter of fact, wind energy is available much wider, unlike solar energy which is not equally available worldwide. It is now highly admitted that wind energy conversion systems are key means to get clean and cheap energy (Li et al. 2019; Goudarzi and Zhu 2013). In large-scale

electrical power generation based on wind turbines, two electric generators outperform over all variable speed machines which are Synchronous Generators (SGs) and DFIGs (Cheng and Zhu 2014). Compared to other machines including SGs, DFIGs offer a number of advantages, e.g., robustness, inexpensiveness, lightweight, the ability to operate at variable speed and the necessity of smaller power converters. In addition, DFIGs allow the control of all the power exchanged with the grid. Finally, DFIGs enable the control of the active power independently from the control of the reactive power (Bektache and Boukhezzar 2018).

In this study, the DFIG-based wind generation system illustrated in Fig. 1 is considered. The stator windings are directly connected to the grid, whereas the rotor windings are coupled to the grid via the rotor side converter (RSC), DC-link capacitor and the grid side converter (GSC) (Kaloi et al. 2016). A number of control techniques have been proposed in literature to get full benefits from the DFIG machine, despite its nonlinearity and model uncertainty. A review of the control strategies for wind energy conversion systems involving DFIG generators is presented in (Mohd Zin et al. 2013). In

✉ Karim Noussi
karim.noussi2@gmail.com

¹ LTI Lab, Faculty of Sciences Ben M'sick, University Hassan II, Casablanca, Morocco

² ESE Lab, ENSEM of Casablanca, University Hassan II, Casablanca, Morocco

³ Normandie Univ, UNICAEN, ENSICAEN, LAC, 14000 Caen, France

⁴ Department of Energy Technology, AAU, 9220 Aalborg East, Denmark

(Noussi et al. 2019; Aguilar et al. 2020; Ko et al. 2008), a classical proportional integral (PI) controller is suggested. Due to its linearity and fixed parameters, a PI controller cannot ensure satisfactory performances over wide range operation conditions. A fuzzy tracking controller is dealt with in Zamzoum et al. (2018); Naik et al. (2020), with some interesting trajectory tracking. Model-based controllers, that account for the nonlinearity of DFIG machine, have been proposed using different design techniques. In Noussi et al. (2020b), a sensorless backstepping controller has been designed to ensure maximum power extraction. A passivity-based control scheme involving parameter estimation was suggested in López-García et al. (2016). A number of controllers, developed using the sliding mode control technique, have been proposed for the control of wind turbine systems. However, these research papers tackle only the control of either the generator connected to RSC or the grid linked to GSC (Beltran et al. 2012; Hu et al. 2011; Yang et al. 2018; Golarany and Moradi 2019; Noussi et al. 2020a). Dealing with the control of the entire DFIG-based energy chain has been subject of some works. As a matter of fact, the power transfer of DFIG-based wind energy systems is ensured by the stator-grid association and the rotor connected to the back-to-back converter-grid association. Since there is an interaction between the different parts of the discussed system, it is crucial to consider the control problem of the whole topology to ensure a smooth power transfer from the wind turbine to the grid (Merabet et al. 2018; Noussi et al. 2021). Authors, in Martinez et al. (2012); Saad et al. (2015), discussed the control of the whole system using the sliding mode technique, including a PI controller that was implemented to regulate the DC-link voltage which does not reject disturbances and cannot handle parametric variations.

Designing adaptive sliding mode controllers for DFIG-based wind energy conversion systems has been dealt with in Barambones et al. (2018); Patnaik and Dash (2015); Sun et al. (2017). Nevertheless, only few research works tackled the adaptive sliding mode control of the whole system depicted in Fig. 1. In Patnaik et al. (2016), authors developed an adaptive sliding mode controller for the complete structure, but they used a linear classical PI controller for the DC-link voltage regulation which is sensitive to parameters' variations. The present paper addresses the control problem considering the complete chain of grid-connected DFIG wind turbine (Fig. 1), using the adaptive sliding mode control technique. The controlled system is able to cope with extra difficulties, including disturbances, unmodeled quantities and parameters' variations caused by temperature, saturation and skin effect. The control design is based on the whole system model that is obtained by applying electrical and physical laws. The resulting adaptive controller turns out to be constituted of several components, including: (i) an MPPT algorithm that determines online the optimal turbine power value in

the sense of maximum energy transfer from the wind to the grid; (ii) a stator powers regulator that makes the DFIG stator active power tracks the optimal value and maintains the stator reactive power at a desired reference; (iii) a DC-link voltage regulator to make energy transfer possible. Then, a theoretical stability analysis is developed proving formally that the adaptive controller actually meets its objectives. The theoretical results are confirmed by several numerical simulations, that also illustrate extra robustness features of the controller.

The paper is organized as follows: In Sect. 2, the mathematical model of DFIG-WECS is developed; Sect. 3 is devoted to the adaptive sliding mode controller design; the stability analysis of the whole closed-loop system is presented in Sect. 4. The performances and robustness of the proposed controller are illustrated by numerical simulation in Sect. 5. Some concluding remarks end the paper.

2 System Description and Modeling

The DFIG-based wind generation system under study is depicted in Fig. 1. Accordingly, the wind turbine is connected to the doubly fed induction generator via the gear box system. The back-to-back voltage source converter is used to ensure the maximum power extraction and guarantee the injection of the active and reactive power into the grid.

2.1 Wind Turbine Model

The mechanical power extracted via the wind turbine is given by Mousa et al. (2019):

$$P_t = \frac{1}{2} \rho \pi R^2 v^3 C_p(\lambda, \beta) \quad (1)$$

where ρ , R , v , C_p are the air density, the rotor radius, the wind speed and the power coefficient, respectively. Moreover, the tip speed ratio can be expressed as:

$$\lambda = \frac{\Omega_t R}{v} \quad (2)$$

where Ω_t is the wind turbine rotor mechanical speed. The power coefficient C_p is given as a function of the pitch angle β and the tip speed ratio λ :

$$C_p(\lambda, \beta) = C_1 \left(\frac{C_2}{\lambda_i} - C_3 \beta - C_4 \beta^{C_5} - C_6 \right) e^{-\frac{C_7}{\lambda_i}} \quad (3)$$

with

$$\lambda_i^{-1} = (\lambda + 0.02\beta)^{-1} - 0.003(\beta^3 + 1)^{-1} \quad (4)$$

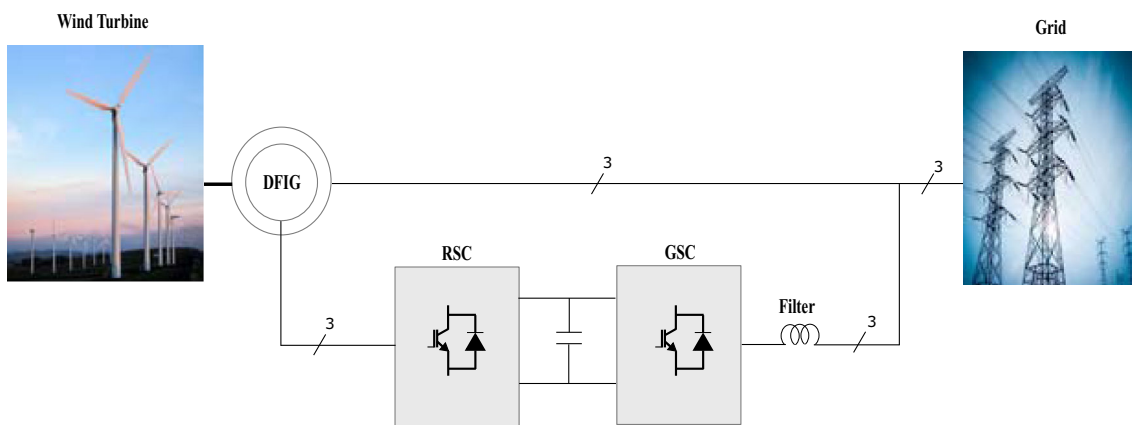


Fig. 1 Simplified scheme of DFIG wind turbine

where the coefficients C_i , ($i = 1, 2, \dots, 7$), have the values: $C_1 = 0.73$, $C_2 = 151$, $C_3 = 0.58$, $C_4 = 0.02$, $C_5 = 2.14$, $C_6 = 13.2$, $C_7 = 18.4$.

2.2 DFIG Dynamic Model

The DFIG voltages in the synchronously rotating reference frame can be expressed as follows (Morawiec et al. 2019; Eshkaftaki et al. 2019; Huang et al. 2019):

$$\begin{pmatrix} v_{sd} \\ v_{sq} \end{pmatrix} = R_s \begin{pmatrix} i_{sd} \\ i_{sq} \end{pmatrix} + \frac{d}{dt} \begin{pmatrix} \phi_{sd} \\ \phi_{sq} \end{pmatrix} + \omega_s \begin{pmatrix} 0 & -1 \\ 1 & 0 \end{pmatrix} \begin{pmatrix} \phi_{sd} \\ \phi_{sq} \end{pmatrix} \tag{5}$$

$$\begin{pmatrix} v_{rd} \\ v_{rq} \end{pmatrix} = R_r \begin{pmatrix} i_{rd} \\ i_{rq} \end{pmatrix} + \frac{d}{dt} \begin{pmatrix} \phi_{rd} \\ \phi_{rq} \end{pmatrix} + \omega_r \begin{pmatrix} 0 & -1 \\ 1 & 0 \end{pmatrix} \begin{pmatrix} \phi_{rd} \\ \phi_{rq} \end{pmatrix} \tag{6}$$

where v_{sdq} , v_{rdq} , i_{sdq} , i_{rdq} , ϕ_{sdq} and ϕ_{rdq} , denote the mean values, over a switching period, of the real signals of the stator and rotor voltages, currents, fluxes in the d–q reference frame, respectively; R_s and R_r are the stator and the rotor resistances; ω_s and ω_r are the synchronous speed of stator flux and the rotor angular frequency, respectively. The stator and the rotor fluxes expressions in the d–q reference frame are given by:

$$\begin{pmatrix} \phi_{sd} \\ \phi_{sq} \\ \phi_{rd} \\ \phi_{rq} \end{pmatrix} = \begin{pmatrix} L_s & 0 & M & 0 \\ 0 & L_s & 0 & M \\ M & 0 & L_r & 0 \\ 0 & M & 0 & L_r \end{pmatrix} \begin{pmatrix} i_{sd} \\ i_{sq} \\ i_{rd} \\ i_{rq} \end{pmatrix} \tag{7}$$

where L_s , L_r and M denote the stator, rotor and mutual inductances, respectively. On the other hand, the stator and the rotor active and reactive powers are given by:

$$P_s = \frac{3}{2} (v_{sd}i_{sd} + v_{sq}i_{sq}) \tag{8a}$$

$$Q_s = \frac{3}{2} (v_{sq}i_{sd} - v_{sd}i_{sq}) \tag{8b}$$

$$P_r = \frac{3}{2} (v_{rd}i_{rd} + v_{rq}i_{rq}) \tag{9a}$$

$$Q_r = \frac{3}{2} (v_{rq}i_{rd} - v_{rd}i_{rq}). \tag{9b}$$

The expression of the generator speed dynamics is written as:

$$J \frac{d\Omega_m}{dt} = C_g - C_{em} - F\Omega_m \tag{10}$$

where $\Omega_m = N\Omega_r$, C_g , $C_t = NC_g$, N , J and F denote the generator speed, high-speed shaft mechanical torque, low-speed shaft mechanical torque, the gear box gain, rotor inertia and the friction coefficient, respectively.

The equation of the electromagnetic torque is defined by:

$$C_{em} = pM (i_{rd}i_{sq} - i_{sd}i_{rq}). \tag{11}$$

2.3 Grid Side Dynamic Model

Applying Kirchhoff’s current law, the current through the DC-link capacitor is given by:

$$i_c = i_{rdc} - i_{gdc}. \tag{12}$$

The powers transferred from the DC-link to the grid side converter are expressed as follows:

$$P_g = \frac{3}{2} (v_{sd}i_{gd} + v_{sq}i_{gq}) \tag{13a}$$

$$Q_g = \frac{3}{2} (v_{sq}i_{gd} - v_{sd}i_{gq}) \tag{13b}$$

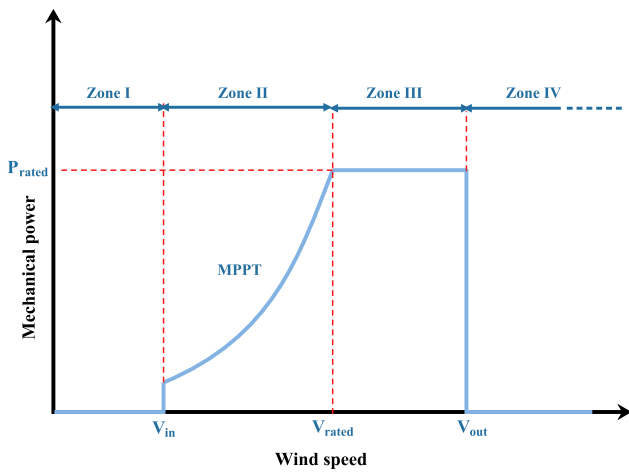


Fig. 2 Wind energy conversion system operating zones

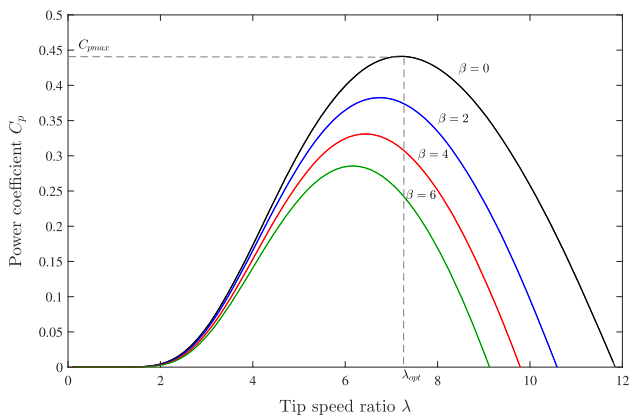


Fig. 3 Power coefficient as a function of tip speed ratio

where i_{gdq} and v_{dc} are the mean values, over a switching period, of the grid side filter currents in the synchronous reference frame and the DC-link voltage, respectively. Assuming that the GSC losses are negligible, the DC-link voltage dynamics are described by the equation (Kim et al. 2016):

$$C_{dc}v_{dc} \frac{dv_{dc}}{dt} = v_{dc}i_{rdc} - P_g \tag{14}$$

The grid side converter voltages in the synchronously rotating reference are expressed as follows:

$$\begin{pmatrix} v_{nd} \\ v_{nq} \end{pmatrix} = R_g \begin{pmatrix} i_{gd} \\ i_{gq} \end{pmatrix} + L_g \frac{d}{dt} \begin{pmatrix} i_{gd} \\ i_{gq} \end{pmatrix} + \begin{pmatrix} v_{sd} \\ v_{sq} \end{pmatrix} + L_g \omega_s \begin{pmatrix} 0 & -1 \\ 1 & 0 \end{pmatrix} \begin{pmatrix} i_{gd} \\ i_{gq} \end{pmatrix} \tag{15}$$

where R_g and L_g are the grid side resistance and inductance, respectively.

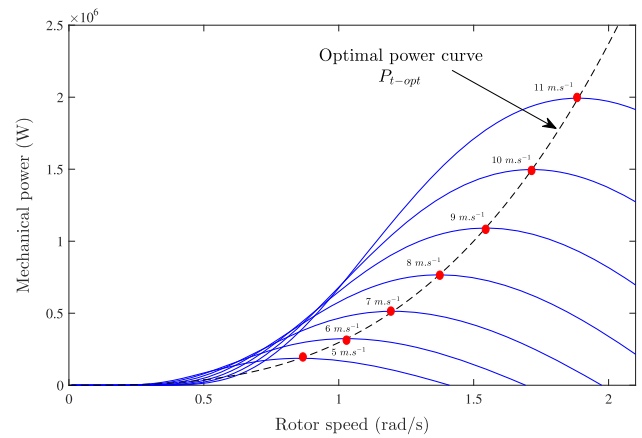


Fig. 4 Mechanical power representation as a function of the rotor speed and wind speed

3 Controller Design

3.1 MPPT Algorithm

It is crucial to include an MPPT loop in the wind system to maximize the available power delivered by the wind turbine (Yang et al. 2016; Falehi and Rafiee 2018; Rezaei 2018). To this end, the present paper addresses the control problem when the wind turbine operates in zone II, see Fig. 2. In this zone, the pitch angle is maintained constant where the controller of the WECS implements the MPPT algorithm to extract the maximum available power during the variations of the wind speed. As this latter increases, the rotor speed increases. When the wind speed becomes more important and the rotor speed reaches its maximum, the wind turbine operates in zone III. In this zone, the aim is to limit the extracted mechanical power. In this case, the mechanical torque should be kept at its nominal value and the pitch angle must be adjusted, thus guaranteeing that the wind turbine operates at the maximum speed and rated power.

The optimal extracted power when the turbine is operating in the maximum power region can be found at optimal values of C_p , λ and β . Using Eqs. (1) and (2) and Fig. 3, the optimal power is given by 16 and represented in Fig. 4 (Zamzoum et al. 2018):

$$P_{t-opt} = \frac{1}{2} \rho \pi \frac{R^5}{\lambda_{opt}^3} C_{pmax} \Omega_r^3 \tag{16}$$

The reference of the stator active power control loop, illustrated in Fig. 5, is retrieved from the difference between the rotor active power (9a) and the output of the MPPT block (16).

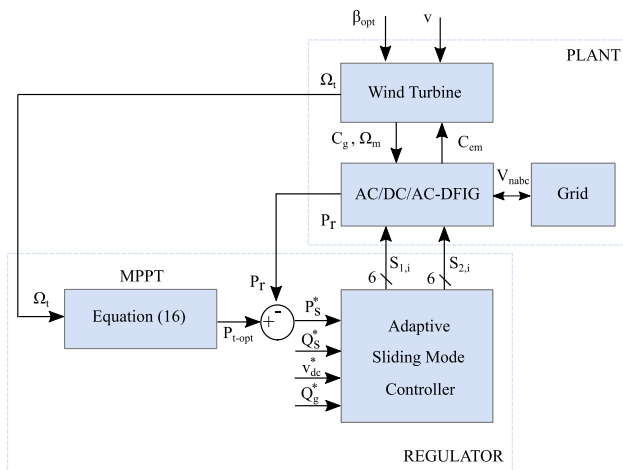


Fig. 5 MPPT Algorithm

3.2 Field Oriented Technique

DFIGs are quite suitable solutions for high power generation requirements, as the generation of electrical power can be fully achieved only from the association of the stator windings and the electrical grid. This entails size reduction of the power converter, as only 20–30% of the rating powers pass through the back-to-back converter. The global extracted power is the sum of the grid side powers and stator powers. In order to simplify the system and power computations, oriented d–q reference frame is applied by adjusting the stator flux so that the quadratic component is null ($\phi_{sd} = \frac{V_s}{\omega_s}$, $\phi_{sq} = 0$) (Golnary and Moradi 2019; Mechter et al. 2016; Xiong et al. 2020). Doing so, the stator voltages equations in (5) get simpler, which together with Eqs. (6) to (8) yields to the following stator powers expressions and the equations of the rotor currents dynamics:

$$P_s = -\frac{3}{2} \frac{M V_s}{L_s} i_{rq} \tag{17a}$$

$$Q_s = -\frac{3}{2} \frac{M V_s}{L_s} \left(i_{rd} - \frac{V_s}{\omega_s M} \right) \tag{17b}$$

$$\frac{di_{rq}}{dt} = \frac{1}{\sigma L_r} \left(\frac{v_{dc}}{2} u_q - R_r i_{rq} - \omega_r \sigma L_r i_{rd} - \omega_r \frac{M \phi_{sd}}{L_s} \right) \tag{18a}$$

$$\frac{di_{rd}}{dt} = \frac{1}{\sigma L_r} \left(\frac{v_{dc}}{2} u_d - R_r i_{rd} + \omega_r \sigma L_r i_{rq} \right). \tag{18b}$$

Similarly, the orientation of the d–q frame simplifies the equations of the grid side powers and the filter current dynamics. Therefore, Eqs. (14) and (15) are rewritten as follows:

$$\frac{dv_{dc}}{dt} = \frac{1}{C_{dc}} \left(i_{rdc} - \frac{3}{2} \frac{V_s}{v_{dc}} i_{gd} \right) \tag{19a}$$

$$\frac{di_{gq}}{dt} = \frac{1}{L_g} \left(\frac{v_{dc}}{2} v_q - R_g i_{gq} - V_s - \omega_s L_g i_{gd} \right) \tag{19b}$$

$$\frac{di_{gd}}{dt} = \frac{1}{L_g} \left(\frac{v_{dc}}{2} v_d - R_g i_{gd} + \omega_s L_g i_{gq} \right). \tag{19c}$$

3.3 Control Objectives

An adaptive sliding mode controller will now be designed for a wind energy conversion system based on DFIG, in order to maximize the produced power and inject it into the grid. There are three main objectives to be simultaneously realized:

- Active power control: ensure that the active power tracks the optimal reference power provided by the MPPT block.
- Reactive power control: maintain the stator and grid side reactive powers equal to zero to guarantee the power factor requirement.
- DC-link regulation: keep the DC-link voltage at a fixed given value.

To meet these objectives, we propose a control scheme consisting of four control loops. A pair of control loops have been used to control the rotor side converter to directly regulate the stator powers, and a pair of control loops have been used to control the grid side converter; one aims at regulating the reactive power by acting on the d-axis current, while the other aims at regulating the DC-link voltage via the q-axis current.

3.4 Rotor Side Controller Design

It is seen in the rotor side reduced model (17) that the stator active power P_s is acted on by the quadrature rotor current i_{rq} , and through the direct current i_{rd} , one can control the stator reactive power Q_s .

Using Eqs. (17) and (18), the derivatives, with powers quantities, yield:

$$\begin{pmatrix} \dot{P}_s \\ \dot{Q}_s \end{pmatrix} = \overbrace{\begin{pmatrix} -\frac{R_r}{\sigma L_r} P_s - \omega_r Q_s + \frac{3\omega_r V_s \phi_{sd}}{2L_s} \left(1 + \frac{M^2}{\sigma L_s L_r} \right) \\ -\frac{R_r}{\sigma L_r} Q_s + \omega_r P_s + \frac{3}{2} \frac{R_r V_s \phi_{sd}}{\sigma L_s L_r} \end{pmatrix}}^{f_r(P_s, Q_s)} + \underbrace{\frac{3}{2} \frac{V_s M}{\sigma L_s L_r} \frac{v_{dc}}{2} \begin{pmatrix} 0 & 1 \\ 1 & 0 \end{pmatrix}}_{D_r} \begin{pmatrix} u_d \\ u_q \end{pmatrix} \tag{20}$$

where the more compact form:

$$\begin{pmatrix} \dot{P}_s \\ \dot{Q}_s \end{pmatrix} = f_r(P_s, Q_s) + D_r u_{dq} \tag{21}$$

$u_{dq} = (u_d \ u_q)^T$ is the control vector of the subsystem (21). The point is that, in practice, the system can face external disturbances (affecting its signals) and parameter uncertainties (affecting its components). Extra unmodeled effects may come into action. Presently, we take in consideration all mentioned modeling errors, by adding uncertainty terms to the two model functions f_r and D_r . Specifically, the latter are rewritten in the form:

$$f_r = f_{r0} + \Delta f_r \tag{22}$$

$$D_r = D_{r0} + \Delta D_r \tag{23}$$

where the modeling errors Δf_r and ΔD_r are assumed to be bounded and f_{r0} and D_{r0} are identical to f_r and D_r , respectively. For convenience, the latter are rewritten:

$$\begin{aligned} f_{r0}(P_s, Q_s) &= \begin{pmatrix} f_{ps}(P_s, Q_s) \\ f_{qs}(P_s, Q_s) \end{pmatrix} \\ &= \begin{pmatrix} \frac{-R_r}{\sigma L_r} P_s - \omega_r Q_s + \frac{3\omega_r V_s \phi_{sd}}{2L_s} \left(1 + \frac{M^2}{\sigma L_s L_r}\right) \\ \frac{-R_r}{\sigma L_r} Q_s + \omega_r P_s + \frac{3}{2} \frac{R_r V_s \phi_{sd}}{\sigma L_s L_r} \end{pmatrix} \end{aligned} \tag{24}$$

$$\begin{aligned} D_{r0} &= \begin{pmatrix} 0 & d_{ps}(v_{dc}) \\ d_{qs}(v_{dc}) & 0 \end{pmatrix} \\ d_{ps}(v_{dc}) &= d_{qs}(v_{dc}) = -\frac{3V_s M v_{dc}}{4\sigma L_s L_r} \end{aligned}$$

Taking into consideration the uncertainty terms, then the expression of the stator powers is rewritten as follows:

$$\begin{pmatrix} \dot{P}_s \\ \dot{Q}_s \end{pmatrix} = f_{r0}(P_s, Q_s) + D_{r0}(v_{dc}) u_{dq} + \Delta_r \tag{25}$$

where $\Delta_r = (\Delta P_s \ \Delta Q_s)^T$ depends on Δf_r and ΔD_r of Eqs. (22) and (23).

To enforce the powers P_s and Q_s to match their references, denoted P_s^* and Q_s^* , we will now design a control law, that generates the control vector u_{dq} , using the sliding mode technique. To this end, we consider the following sliding surfaces:

$$S_r = \begin{pmatrix} S_{P_s} \\ S_{Q_s} \end{pmatrix} = \begin{pmatrix} e_{P_s} + k_1 \int_0^t e_{P_s}(\tau) d\tau \\ 0 \\ e_{Q_s} + k_2 \int_0^t e_{Q_s}(\tau) d\tau \end{pmatrix} \tag{26}$$

where

$$\begin{pmatrix} e_{P_s} \\ e_{Q_s} \end{pmatrix} = \begin{pmatrix} P_s - P_s^* \\ Q_s - Q_s^* \end{pmatrix} \tag{27}$$

and k_1, k_2 are positive real design parameters .

The additional integral terms on the right side of (26) are introduced to ensure zero steady-state errors.

The dynamics of the chosen sliding surfaces are expressed as:

$$\dot{S}_r = \begin{pmatrix} \dot{S}_{P_s} \\ \dot{S}_{Q_s} \end{pmatrix} = \begin{pmatrix} \dot{e}_{P_s} + k_1 e_{P_s} \\ \dot{e}_{Q_s} + k_2 e_{Q_s} \end{pmatrix}. \tag{28}$$

Using (25)–(27), the time derivative of the sliding surfaces is given by:

$$\dot{S}_r = \begin{pmatrix} k_1 e_{P_s} - \dot{P}_s^* \\ k_2 e_{Q_s} - \dot{Q}_s^* \end{pmatrix} + f_{r0}(P_s, Q_s) + D_{r0} u_{dq} + \Delta_r. \tag{29}$$

According to the sliding mode control principle (Barambones et al. 2018), the control signal is described as $u_{dq} = u_{dq}^{a0} + u_{dq}^{as}$, where u_{dq}^{a0} denotes the nominal control law, which keeps the system on the sliding surface, and u_{dq}^{as} is the adaptive switching control law, which contains both a discontinuous component that is responsible for inducing sliding motion on the surface and an adaptive gain that compensates the lumped uncertainty terms.

Thus, the sliding mode vector control law for stator powers can be obtained as follows:

$$u_{dq} = -D_{r0}^{-1} \left[\overbrace{\begin{pmatrix} k_1 e_{P_s} - \dot{P}_s^* \\ k_2 e_{Q_s} - \dot{Q}_s^* \end{pmatrix}}^{u_{dq}^{a0}} + f_{r0}(P_s, Q_s) + \underbrace{\begin{pmatrix} \hat{\zeta}_1 \operatorname{sgn}(S_{P_s}) \\ \hat{\zeta}_2 \operatorname{sgn}(S_{Q_s}) \end{pmatrix}}_{u_{dq}^{as}} \right]. \tag{30}$$

Accordingly, the dynamics of the estimated switching gains can be suggested as :

$$\dot{\hat{\zeta}}_1 = \frac{1}{\gamma_1} |S_{P_s}| \tag{31}$$

$$\dot{\hat{\zeta}}_2 = \frac{1}{\gamma_2} |S_{Q_s}| \tag{32}$$

where γ_i are positive real gains, and $\hat{\zeta}_i$ denote the estimated adaptation gains which act as adjustable values of the adaptive switching control law gains, ($i = 1, 2$). The adaptation speed of $\hat{\zeta}_i$ can be tuned by γ_i , ($i = 1, 2$). The estimation error is defined by Katir et al. (2021):

$$\tilde{\zeta}_i = \hat{\zeta}_i - \zeta_i. \tag{33}$$

3.5 Grid Side Controller Design

The controller of the grid side converter is expected to achieve two main objectives: (i) ensuring a tight regulation of the DC-link voltage (this guarantees a suitable transmission of the power flowing through the rotor of the generator); (ii) controlling the reactive power exchanged with the grid. The controller we are proposing consists of two loops; the first loop aims at regulating the DC bus voltage based on the q-axis filter current, the second loop aims at controlling the grid side reactive power through the d-axis filter current. The tracking error of the DC-link voltage and the d-axis current can be defined as follows:

$$\begin{pmatrix} e_{id} \\ e_v \end{pmatrix} = \begin{pmatrix} i_{gd} - i_{gd}^* \\ v_{dc} - v_{dc}^* \end{pmatrix}. \tag{34}$$

Using (19), the time derivative of equation (34) yields:

$$\begin{pmatrix} \dot{e}_{id} \\ \dot{e}_v \end{pmatrix} = \begin{pmatrix} \frac{1}{L_g} \left(\frac{v_{dc}}{2} v_d - R_g i_{gd} + \omega_s L_g i_{gq} \right) - \dot{i}_{gd}^* \\ \frac{1}{C_{dc}} \left(i_{rdc} - \frac{3}{2} \frac{V_s}{v_{dc}} i_{gq} \right) - \dot{v}_{dc}^* \end{pmatrix}. \tag{35}$$

We define the sliding surfaces as:

$$S_g = \begin{pmatrix} S_{id} \\ S_v \end{pmatrix} = \begin{pmatrix} e_{id} + k_3 \int_0^t e_{id}(\tau) d\tau \\ \dot{e}_v + \varsigma_0 e_v + k_4 \int_0^t e_v(\tau) d\tau \end{pmatrix} \tag{36}$$

k_3 and k_4 are positive real design parameters. The choice of the sliding surface S_v is motivated by the fact that the relative degree of the system is $n = 2$, where the general form is written as:

$$S_x = \left(\frac{d}{dt} + \varsigma_0 \right)^{n-1} e_x. \tag{37}$$

The time derivative of the sliding surfaces is given by:

$$\dot{S}_g = \begin{pmatrix} \dot{S}_{id} \\ \dot{S}_v \end{pmatrix} = \begin{pmatrix} \dot{e}_{id} + k_3 e_{id} \\ \ddot{e}_v + \varsigma_0 \dot{e}_v + k_4 e_v \end{pmatrix}. \tag{38}$$

Using (35), the time derivative of (36) is written as:

$$\begin{aligned} \dot{S}_g = & \begin{pmatrix} k_3 e_{id} - \dot{i}_{gd}^* \\ k_4 e_v - \varsigma_0 \dot{v}_{dc}^* - \ddot{v}_{dc}^* \end{pmatrix} + f_{g0}(v_{dc}, i_{gd}, i_{gq}) \\ & + D_{g0} \cdot v_{dq} + \Delta_g \end{aligned} \tag{39}$$

with

$$\Delta_g = \begin{pmatrix} \Delta_{id} \\ \Delta_v \end{pmatrix} = \begin{pmatrix} \Delta f_{id} + \Delta d_{id} \cdot v_d \\ \Delta f_v + \Delta d_v \cdot v_q + \frac{1}{C_{dc}} i_{rdc} + \frac{\varsigma_0}{C_{dc}} i_{rdc} \end{pmatrix}. \tag{40}$$

Note that all uncertain terms are gathered in Δ_g , including the current i_{rdc} which is considered as an external disturbance. The remaining quantities on the right side of (39) are defined as follows:

$$\begin{aligned} f_{g0}(v_{dc}, i_{gd}, i_{gq}) &= \begin{pmatrix} f_{id}(v_{dc}, i_{gd}, i_{gq}) \\ f_v(v_{dc}, i_{gd}, i_{gq}) \end{pmatrix} \\ &= \begin{pmatrix} -R_g i_{gd} + \omega_s L_g i_{gq} \\ \frac{3}{2} \frac{V_s}{C_{dc} v_{dc} L_g} (R_g i_{gq} + \omega_s L_g i_{gd} + V_s) \end{pmatrix} \end{aligned} \tag{41}$$

$$D_{g0} = \begin{pmatrix} \frac{v_{dc}}{2L_g} & 0 \\ 0 & \frac{-3V_s}{4C_{dc}L_g} \end{pmatrix} \tag{42}$$

$$v_{dq} = (v_d \ v_q)^T. \tag{43}$$

It can be seen from (39) that the nominal control law appears in the first derivative of the sliding surface. Thus, $v_{dq}^{a0} = v_{dq}$ is obtained from the invariance of the surface $S_g = \dot{S}_g = 0$. As in the previous subsection, an adaptive switching control law is proposed. Then, the global adaptive control law can be written as follows:

$$\begin{aligned} v_{dq} = & -D_{g0}^{-1} \left[\overbrace{\begin{pmatrix} k_3 e_{id} - \dot{i}_{gd}^* \\ k_4 e_v - \varsigma_0 \dot{v}_{dc}^* - \ddot{v}_{dc}^* \end{pmatrix}}^{v_{dq}^{a0}} + f_{g0}(v_{dc}, i_{gd}, i_{gq}) \right. \\ & \left. + \underbrace{\begin{pmatrix} \hat{\zeta}_3 \operatorname{sgn}(S_{id}) \\ \hat{\zeta}_4 \operatorname{sgn}(S_v) \end{pmatrix}}_{v_{dq}^{as}} \right] \end{aligned} \tag{44}$$

where the dynamics of the estimated switching gains can be expressed as follows:

$$\dot{\zeta}_3 = \frac{1}{\gamma_3} |S_{id}| \tag{45}$$

$$\dot{\zeta}_4 = \frac{1}{\gamma_4} |S_v| \tag{46}$$

where γ_3 and γ_4 are positive real gains. Finally, the complete controller design for stator powers, DC-link voltage and grid side reactive power is established. For convenience, the whole established controller is summarized in Table 1.

4 System Stability Analysis

The stability analysis plays a crucial role in the control theory (Aourir et al. 2020). In this section, the Lyapunov stability

Table 1 Recapitulation of the whole proposed adaptive controller

Optimal power reference algorithm:

$$P_{l-opt} = \frac{1}{2} \rho \pi \frac{R^5}{\lambda_{opt}^3} C_{pmax} \Omega_r^3$$

Stator powers adaptive sliding mode control laws:

$$u_{dq} = -D_{r0}^{-1} \left[\begin{pmatrix} k_1 e_{P_s} - \dot{P}_s^* \\ k_2 e_{Q_s} - \dot{Q}_s^* \end{pmatrix} + f_{r0}(P_s, Q_s) + \begin{pmatrix} \hat{\zeta}_1 \operatorname{sgn}(S_{P_s}) \\ \hat{\zeta}_2 \operatorname{sgn}(S_{Q_s}) \end{pmatrix} \right]$$

Grid side adaptive sliding mode control laws:

$$v_{dq} = -D_{g0}^{-1} \left[\begin{pmatrix} k_3 e_{i_d} - \dot{i}_{gd}^* \\ k_4 e_v - \dot{v}_{dc}^* - \ddot{v}_{dc}^* \end{pmatrix} + f_{g0}(v_{dc}, i_{gd}, i_{gq}) + \begin{pmatrix} \hat{\zeta}_3 \operatorname{sgn}(S_{i_d}) \\ \hat{\zeta}_4 \operatorname{sgn}(S_v) \end{pmatrix} \right]$$

approach will be used in the proof of the next theorem to investigate the stability of the whole closed-loop system.

The following two assumptions will be needed for the trajectory tracking:

- A1) The uncertainties of the system are bounded, i.e., $|\Delta_x| \leq \Delta_{x \max}$, $x \in \{P_s, Q_s, i_d, v\}$, where Δ_x refers to the lumped uncertainties in Δ_r and Δ_g .
- A2) It is required that the switching gains verify $\zeta_i \geq \Delta_{x \max}$ with $x \in \{P_s, Q_s, i_d, v\}$ and $(i = 1, 2, 3, 4)$.

Theorem 1 Consider the global control system illustrated in Fig. 6 and composed of: (i) the wind turbine model (1)–(4), DFIG-AC/DC association model (5)–(8) and grid side system model (5)–(15) which are subject to assumption A1; (ii) the rotor side and grid side controllers of Table 1 that are subject to assumption A2, where the design parameters $(k_1, k_2, k_3, k_4, \gamma_1, \gamma_2, \gamma_3, \gamma_4)$ are positive real constants. Then, the resulting closed-loop system with state variables $(S_r, \tilde{\zeta}_1, \tilde{\zeta}_2, S_g, \tilde{\zeta}_3, \tilde{\zeta}_4)$ is finite time stable and S_r and S_g converge to zero.

Proof For convenience, the time derivatives of the sliding surfaces of the controllers on both sides can be represented using the following compact form:

$$\dot{S}_x = -\hat{\zeta}_i \operatorname{sgn}(S_x) + \Delta_x \quad \text{with} \quad x \in \{P_s, Q_s, i_d, v\} \quad \text{and} \quad (i = 1, 2, 3, 4). \quad (47)$$

Consider the Lyapunov function candidate

$$V_c = \frac{1}{2} S_{P_s}^2 + \frac{1}{2} S_{Q_s}^2 + \frac{1}{2} S_{i_d}^2 + \frac{1}{2} S_v^2 + \frac{1}{2} \sum_{i=1}^4 \gamma_i \tilde{\zeta}_i^2. \quad (48)$$

Using (47), the time derivative of (48) results to be:

$$\begin{aligned} \dot{V}_c = & -\hat{\zeta}_1 |S_{P_s}| - \hat{\zeta}_2 |S_{Q_s}| - \hat{\zeta}_3 |S_{i_d}| - \hat{\zeta}_4 |S_v| \\ & + \Delta_{P_s} S_{P_s} + \Delta_{Q_s} S_{Q_s} + \Delta_{i_d} S_{i_d} + \Delta_v S_v + \sum_{i=1}^4 \gamma_i \tilde{\zeta}_i \dot{\zeta}_i. \end{aligned} \quad (49)$$

Taking into account that $\dot{\zeta}_i = -\dot{\zeta}_i$, $(i = 1, 2, 3, 4)$, and substituting the dynamics of the adaptive gains of (31), (32), (45) and (46) into (49), we obtain :

$$\begin{aligned} \dot{V}_c = & -\zeta_1 |S_{P_s}| - \zeta_2 |S_{Q_s}| - \zeta_3 |S_{i_d}| - \zeta_4 |S_v| \\ & + \Delta_{P_s} S_{P_s} + \Delta_{Q_s} S_{Q_s} + \Delta_{i_d} S_{i_d} + \Delta_v S_v. \end{aligned} \quad (50)$$

According to assumption A1, the following inequality applies

$$\dot{V}_c \leq (-\zeta_m + 4\Delta_M) (|S_{P_s}| + |S_{Q_s}| + |S_{i_d}| + |S_v|) \quad (51)$$

where

$$\begin{aligned} \zeta_m = & \min(\zeta_1, \zeta_2, \zeta_3, \zeta_4), \\ \Delta_M = & \max(|\Delta_{P_s \max}|, |\Delta_{Q_s \max}|, |\Delta_{i_d \max}|, |\Delta_{v \max}|). \end{aligned}$$

Using the next inequality, for $0 < \alpha < 2$

$$\sum_{i=1}^n |\vartheta_i|^\alpha \geq \left(\sum_{i=1}^n \vartheta_i^2 \right)^{\frac{\alpha}{2}}. \quad (52)$$

Equation (51) becomes:

$$\dot{V}_c \leq -\partial_0 V_c \quad (53)$$

where $\partial_0 = \sqrt{2}(\zeta_m - 4\Delta_M)$.

Finally, the integral of (53) over the time interval $0 \leq \tau \leq t$, yields:

$$\sqrt{V_c} \leq -\frac{1}{2} \partial_0 t + \sqrt{V_c(t_0)}. \quad (54)$$

In view of assumption A2, it follows that $\partial_0 \geq 0$. Therefore, the system with state variables $(S_x, \tilde{\zeta}_i)$ is stable and S_x converge to zero in finite time. The convergence time of the closed-loop system is calculated as $T(t_0) \leq \frac{2}{\partial_0} \sqrt{V_c(t_0)}$. This end the proof. \square

Remark 1 In order to reduce the chattering effect produced by the signum function $\operatorname{sgn}(\cdot)$, a sigmoid $\tanh(\cdot)$ function is used instead of $\operatorname{sgn}(\cdot)$ as suggested in Abouloifa et al. (2018).

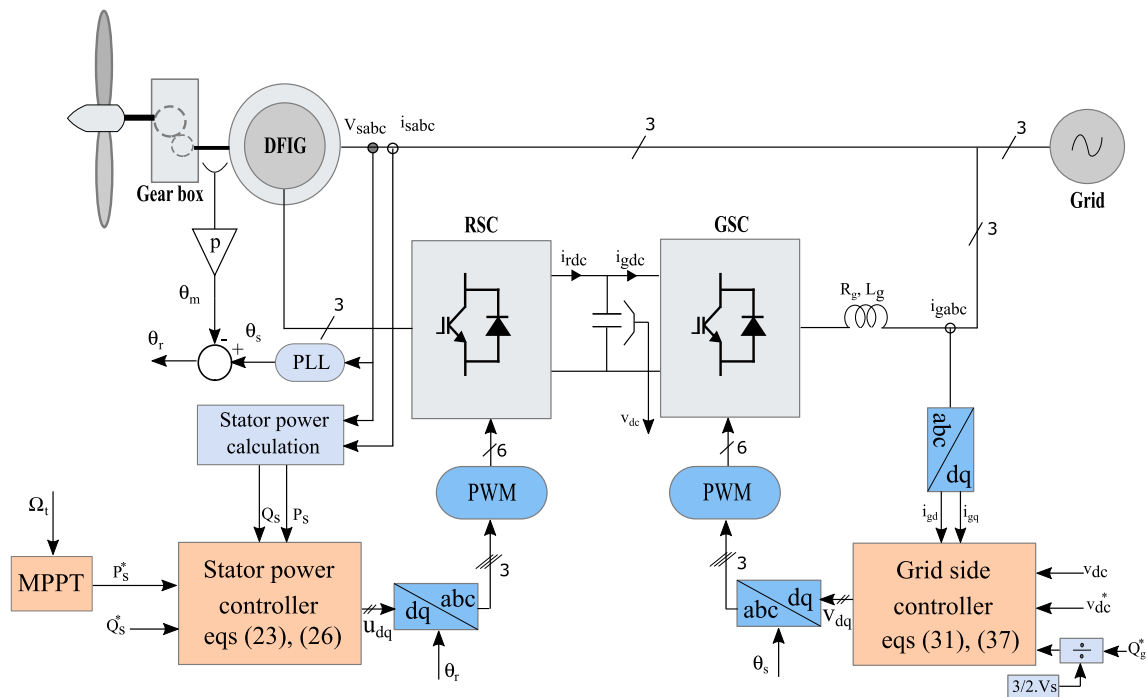


Fig. 6 Overall control scheme of DFIG wind turbine

Table 3 Controller parameters

Parameters	Symbols	Values
MPPT	C_{pmax}, λ_{opt}	0.44, 7.2
Rotor side controller	$k_1, k_2, \gamma_1, \gamma_2$	0.1, 0.1, 10, 100
Grid side controller	$k_3, k_4, \gamma_3, \gamma_4, \varsigma_0$	0.1, 0.1, 250, 10, 300

Table 2 Wind turbine parameters

Parameters	Symbol	Value	Unit
Turbine	N	100	–
	R	42	m
	ρ	1.1225	Kg m^3
	v_{rated}	12.5	m s^{-1}
	$v_{in-vout}$	5–15	m s^{-1}
	$\Omega_{tmin} - \Omega_{tmax}$	9–18	rpm
Network	V_n/U_n	400/690	V
	f	50	Hz
AC/DC/AC converters	R_g	0.02	$\text{m}\Omega$
	L_g	0.4	mH
	C	80	mF
DFIG machine	v_{dc}	1150	V
	P_n	2	MW
	R_s/R_r	2.6/2.9	$\text{m}\Omega$
	L_s/L_r	26	mH
	M	2.5	mH
	$\Omega_{mmin} - \Omega_{mmax}$	900–2000	rpm

5 Simulation Results and Interpretations

The simulation of the studied 2MW DFIG-based wind generation system of Fig. 6 is carried out using MATLAB/Simulink/ SimPowerSystems environment. Numerical simulation is resorted not only to check the theoretical results of Theorem 1, but also to emphasize extra robustness features of the controller. The simulation study is performed by successively considering the following operating conditions:

- (1) Fixed wind speed changes
- (2) Variable wind speed changes
- (3) Robustness under DFIG parameters uncertainties
- (4) Robustness under voltage dips

The DFIG-based wind generation parameters are shown in Table 2. The controller parameters shown in Table 3 have proved to be appropriate based on trial-and-error search.

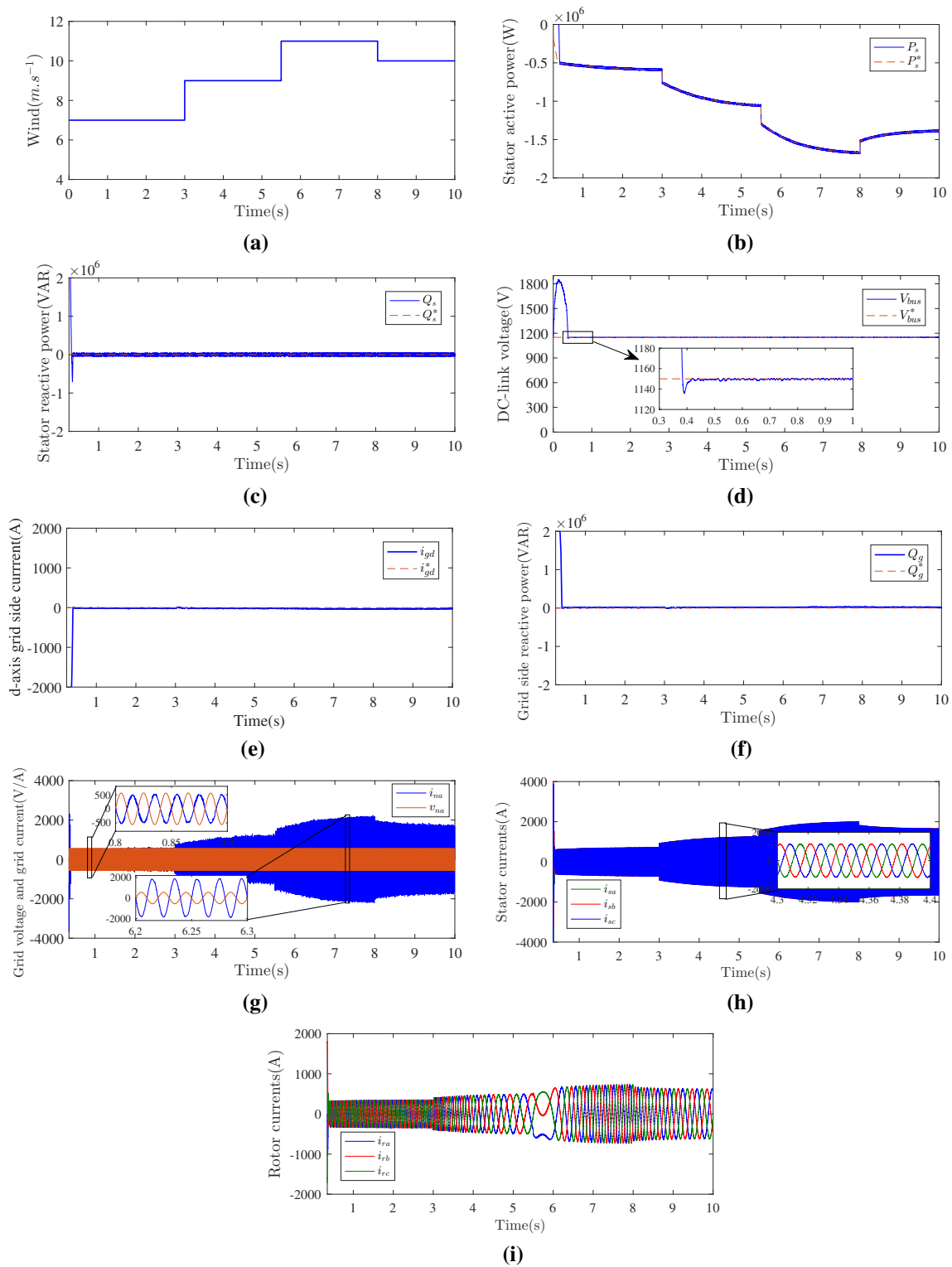


Fig. 7 Obtained results under fixed wind speed changes (solid line: regulated signals; dotted line: their reference trajectories)

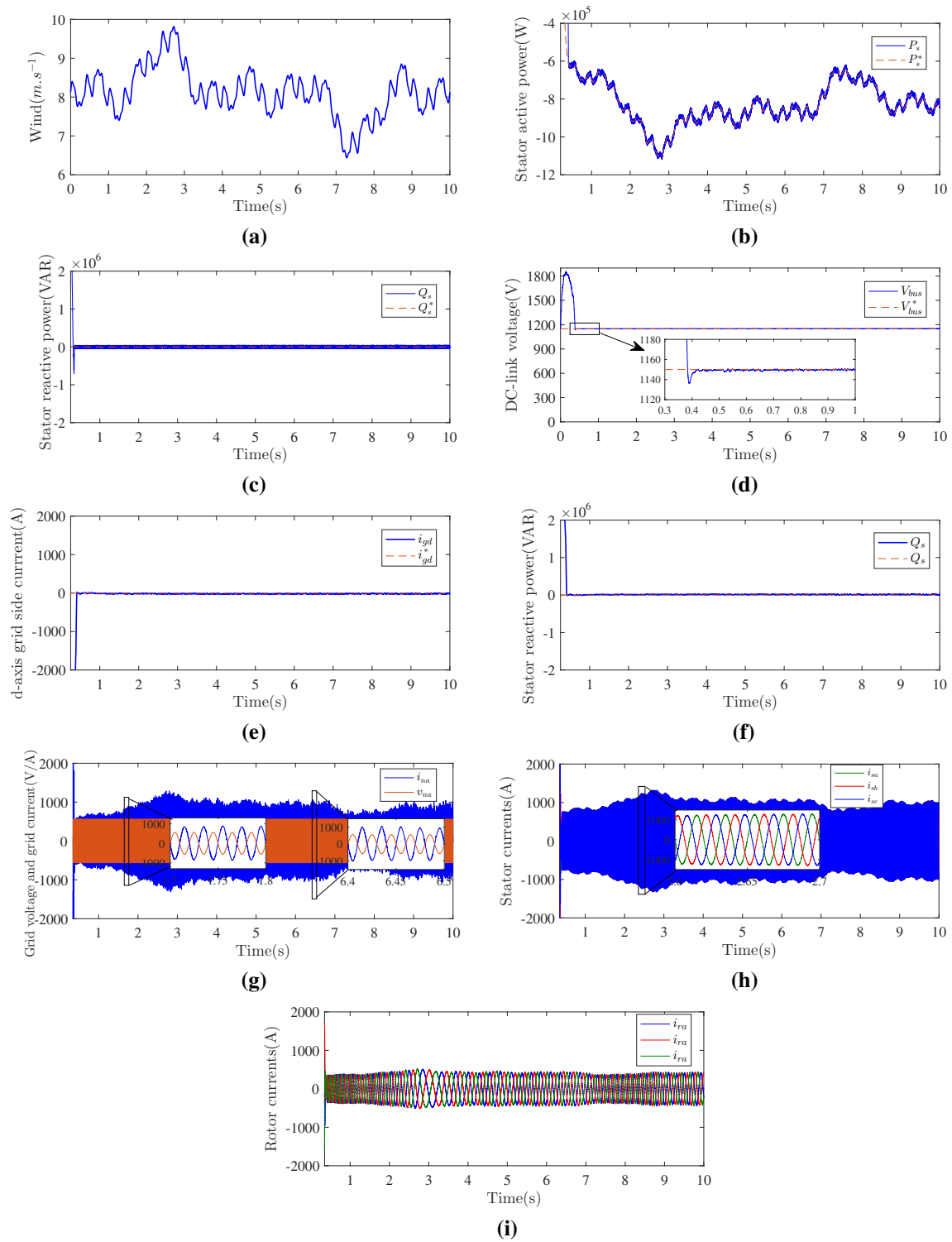


Fig. 8 Obtained results under variable wind speed changes (solid line: regulated signals; dotted line: their reference trajectories)

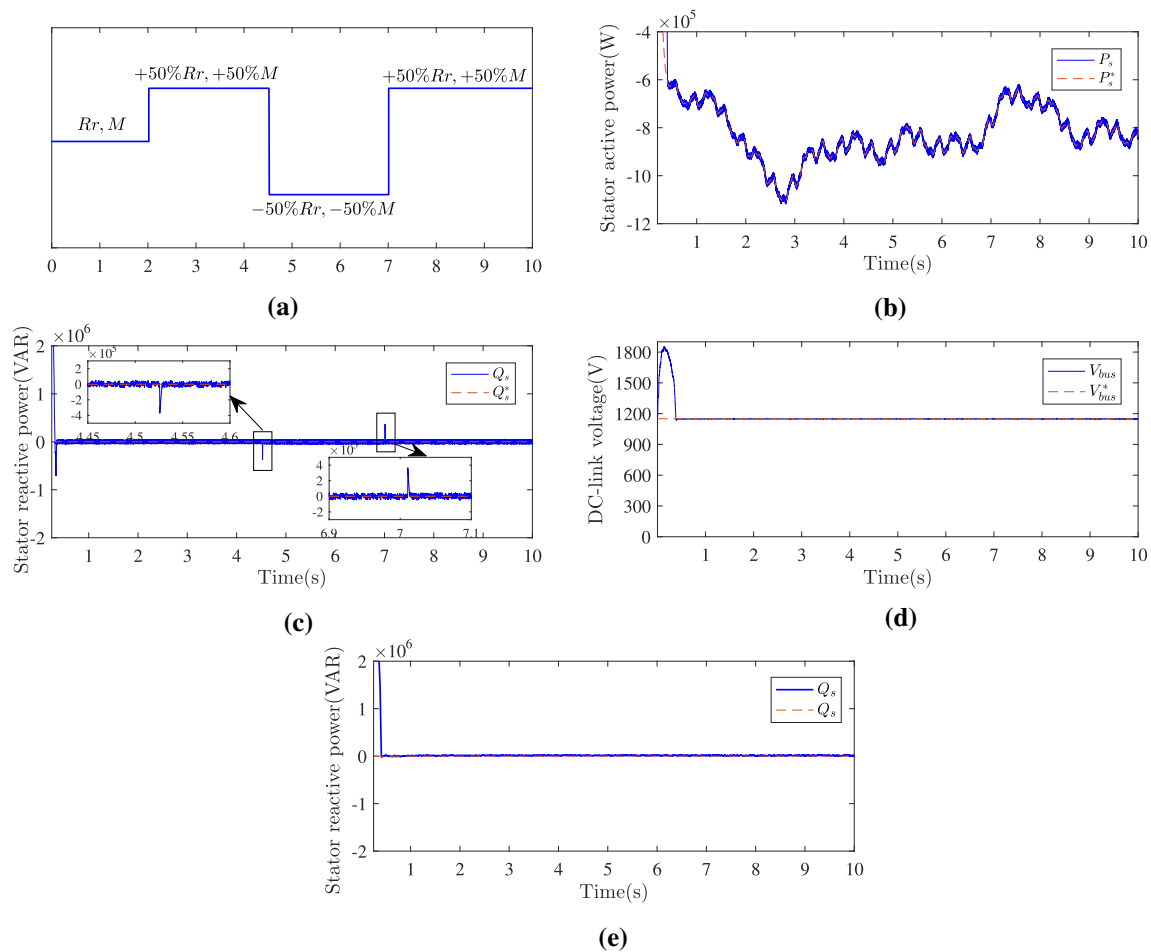


Fig. 9 Controller robustness under DFIG parameters' uncertainty (solid line: regulated signals; dotted line: their reference trajectories)

5.1 Fixed Wind Speed

The simulation protocol is such that the wind velocity takes four different values (6.5, 8.5, 10.5, 9)m/s. These velocity values hold successively on the intervals [0, 3[s, [3, 5.5[s, [5.5, 8[s and [8, 10[s, see Fig. 7a.

Figure 7b shows that the stator active power delivered by the wind power conversion system tracks exactly the optimal reference delivered by the MPPT block. Fig. 7c confirms that the stator reactive power rapidly vanishes which guarantees the achievement of the unitary power factor objective, see also Fig. 7g. The tight regulation of the DC-link voltage to a constant value is shown in Fig. 7d. The d-axis filter current, stator currents and the rotor currents are depicted in Fig. 7e, h and i, respectively.

5.2 Variable Wind Speed

To check the ability of the adaptive SMC controller to regulate the powers, under realistic wind speed fluctuations, a random wind speed is chosen as depicted in Fig. 8a with

an average speed of 8 m/s. From Fig. 8b–i, it is seen that the proposed adaptive controller performs well despite the changes of the wind. As seen in Fig. 8b, the active power tracks precisely the suggested reference value. Also, Fig. 8c shows that the reactive power converges to zero. On the other hand, the DC-link voltage and direct axis current track their respective references despite the severe wind variations, see Fig. 8d–e. Stator and rotor currents are depicted in Fig. 8h–i, respectively.

5.3 Robustness Tests

To check the robustness of the proposed adaptive controller, two interesting tests are considered: parameters' uncertainties and grid fault.

5.3.1 Robustness Under DFIG Parameters Uncertainties

In this case study, the rotor resistances and the mutual inductance are subject to variations, reflecting, e.g., the skin effect

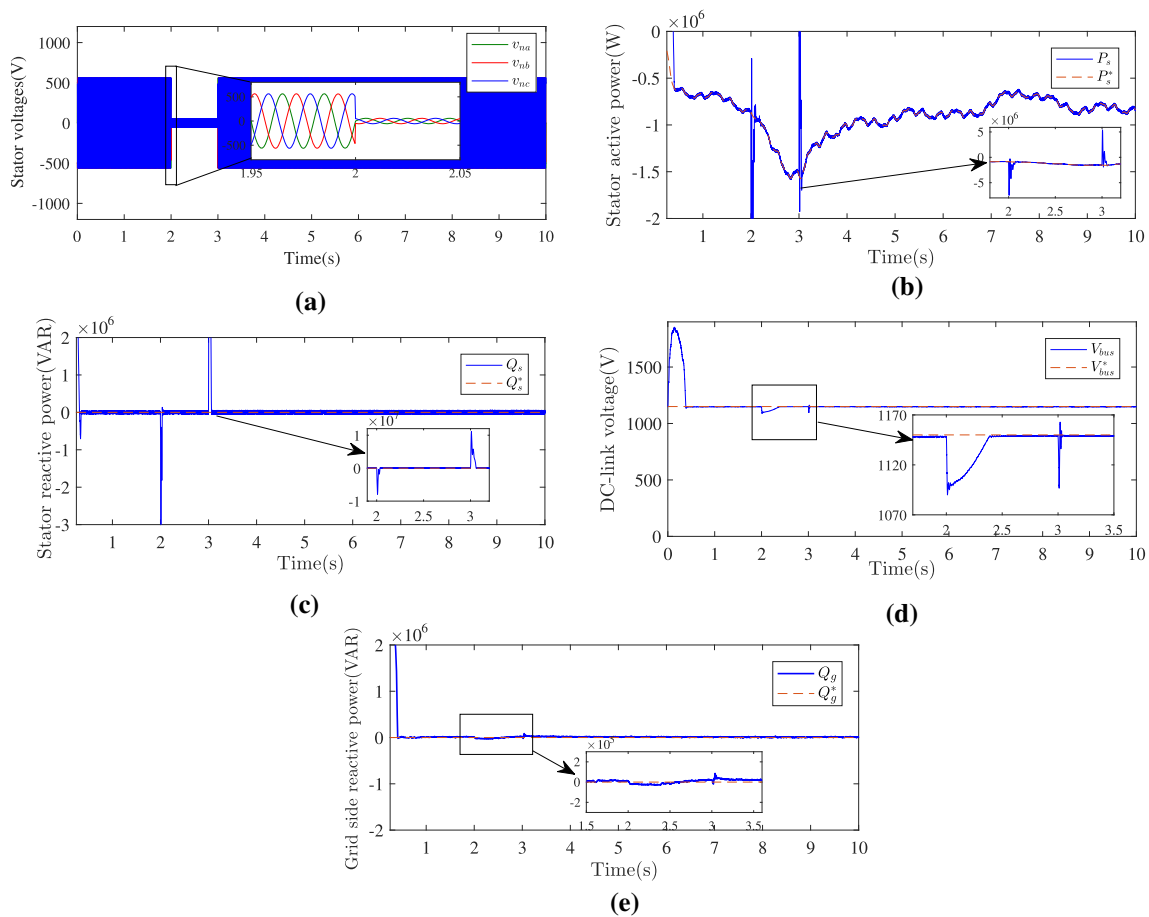


Fig. 10 Controller robustness under voltage dips (solid line: regulated signals; dotted line: their reference trajectories)

Table 4 Parameters variation

Time-span	[0 2]	[2 4.5]	[4.5 7]	[7 10]
Rotor resistances	R_r	$R_r + \frac{R_r}{2}$	$R_r - \frac{R_r}{2}$	$R_r + \frac{R_r}{2}$
Mutual inductance	M	$M + \frac{M}{2}$	$M - \frac{M}{2}$	$M + \frac{M}{2}$

phenomenon and magnetic saturation problem. These variations are detailed in Table 4 and illustrated in Fig. 10a.

Figure 10b–e shows a satisfactory robustness of the proposed adaptive SMC controller. Actually, the output reference tracking objectives are still satisfactorily achieved despite the parameters R_r and M uncertainties. Figure 10b shows that the stator active power tracks well its reference signal despite the DFIG parameters’ changes. These latter cause a slight overshooting as it can be seen in the curve of the stator reactive power displayed in Fig. 10c. Figure 10d shows that the DC-link voltage is maintained at the desired value despite the made variations.

5.3.2 Robustness Under Voltage Dips

Fig. 9a shows a voltage dips of 90%. Figure 9b–e illustrates the capability of the proposed controller to face grid faults and maintain satisfactory tracking performances.

6 Conclusion

We have considered the problem of controlling the powers of a wind turbine system based on DFIG (Fig. 1). The problem has been addressed using the adaptive sliding mode control technique leading to the design of an adaptive regulator (Table 1). The controlled system has been analyzed in Theorem 1 using Lyapunov stability tools. The theoretical results have been confirmed by numerical simulations which also emphasized extra robustness properties.

References

Abouloifa, A., Aouadi, C., Lachkar, I., Boussairi, Y., Aourir, M., & Hamdoun, A. (2018). Output-feedback nonlinear adaptive control strategy of the single-phase grid-connected photovoltaic system.

- Journal of Solar Energy*, 2018, 1–14. <https://doi.org/10.1155/2018/6791056>.
- Aguilar, M. E. B., Coury, D. V., Reginatto, R., & Monaro, R. M. (2020). Multi-objective pso applied to pi control of dfig wind turbine under electrical fault conditions. *Electric Power Systems Research*, 180, 106081. <https://doi.org/10.1016/j.epsr.2019.106081>.
- Aourir, M., Abouloifa, A., Lachkar, I., Aouadi, C., Giri, F., & Guerrero, J. M. (2020). Nonlinear control and stability analysis of single stage grid-connected photovoltaic systems. *International Journal of Electrical Power & Energy Systems*, 115, 105439. <https://doi.org/10.1016/j.ijepes.2019.105439>.
- Barambones, O., Gonzalez de Durana, J., & Calvo, I. (2018). Adaptive sliding mode control for a double fed induction generator used in an oscillating water column system. *Energies*, 11(11), 2939. <https://doi.org/10.3390/en11112939>.
- Bektache, A., & Boukhezzar, B. (2018). Nonlinear predictive control of a DFIG-based wind turbine for power capture optimization. *International Journal of Electrical Power & Energy Systems*, 101, 92–102. <https://doi.org/10.1016/j.ijepes.2018.03.012>.
- Beltran, B., Benbouzid, M. E. H., & Ahmed-Ali, T. (2012). Second-order sliding mode control of a doubly fed induction generator driven wind turbine. *IEEE Transactions on Energy Conversion*, 27(2), 261–269.
- Cheng, M., & Zhu, Y. (2014). The state of the art of wind energy conversion systems and technologies: A review. *Energy Conversion and Management*, 88, 332–347. <https://doi.org/10.1016/j.enconman.2014.08.037>.
- Eshkaftaki, A. A., Rabiee, A., Kargar, A., & Boroujeni, S. T. (2019). An applicable method to improve transient and dynamic performance of power system equipped with dfig-based wind turbines. *IEEE Transactions on Power Systems*, 35(3), 2351–2361. <https://doi.org/10.1109/TPWRS.2019.2954497>.
- Falehi, A. D., & Rafiee, M. (2018). Maximum efficiency of wind energy using novel dynamic voltage restorer for dfig based wind turbine. *Energy Reports*, 4, 308–322. <https://doi.org/10.1016/j.egy.2018.01.006>.
- Golnary, F., & Moradi, H. (2019). Dynamic modelling and design of various robust sliding mode controls for the wind turbine with estimation of wind speed. *Applied Mathematical Modelling*, 65, 566–585. <https://doi.org/10.1016/j.apm.2018.08.030>.
- Goudarzi, N., & Zhu, W. D. (2013). A review on the development of wind turbine generators across the world. *International Journal of Dynamics and Control*, 1(2), 192–202. <https://doi.org/10.1007/s40435-013-0016-y>.
- Huang, S., Wu, Q., Guo, Y., & Rong, F. (2019). Optimal active power control based on mpc for dfig-based wind farm equipped with distributed energy storage systems. *International Journal of Electrical Power & Energy Systems*, 113, 154–163. <https://doi.org/10.1016/j.ijepes.2019.05.024>.
- Hu, J., Shang, L., He, Y., & Zhu, Z. Q. (2011). Direct active and reactive power regulation of grid-connected DC/AC converters using sliding mode control approach. *IEEE Transactions on Power Electronics*, 26(1), 210–222. <https://doi.org/10.1109/TPEL.2010.2057518>.
- Kaloi, G. S., Wang, J., & Baloch, M. H. (2016). Active and reactive power control of the doubly fed induction generator based on wind energy conversion system. *Energy Reports*, 2, 194–200. <https://doi.org/10.1016/j.egy.2016.08.001>.
- Katir, H., Abouloifa, A., Lachkar, I., Noussi, K., Giri, F., & Guerrero, J. (2020). Advanced nonlinear control of a grid-connected photovoltaic power system using n-cascaded h-bridge multilevel inverters. *IFAC-PapersOnLine*, 53(2), 12859–12864. <https://doi.org/10.1016/j.ifacol.2020.12.2095>.
- Katir, H., Abouloifa, A., Noussi, K., Lachkar, I., & Giri, F. (2021). Cascaded h-bridge inverters for ups applications: Adaptive backstepping control and formal stability analysis. *IEEE Control Systems Letters*. <https://doi.org/10.1109/LCSYS.2021.3051875>.
- Kim, H. W., Kim, H., Kwon, S., & Choi, J. Y. (2016). Robust backstepping controller for grid-side converter of dfig-based wind energy conversion systems. *IEEE Transactions on Electrical and Electronic Engineering*, 11(5), 633–639. <https://doi.org/10.1002/tee.22281>.
- Ko, H. S., Yoon, G. G., Kyung, N. H., & Hong, W. P. (2008). Modeling and control of dfig-based variable-speed wind-turbine. *Electric Power Systems Research*, 78(11), 1841–1849. <https://doi.org/10.1016/j.epsr.2008.02.018>.
- Li, P., Xiong, L., Wu, F., Ma, M., & Wang, J. (2019). Sliding mode controller based on feedback linearization for damping of sub-synchronous control interaction in dfig-based wind power plants. *International Journal of Electrical Power & Energy Systems*, 107, 239–250. <https://doi.org/10.1016/j.ijepes.2018.11.020>.
- López-García, I., Beltran-Carbajal, F., Espinosa-Pérez, G., & Escarela-Perez, R. (2016). Passivity-based power control of a doubly fed induction generator with unknown parameters: PASIVITY OF DFIM GENERATOR. *International Transactions on Electrical Energy Systems*, 26(11), 2402–2424. <https://doi.org/10.1002/etep.2213>.
- Martinez, M. I., Tapia, G., Susperregui, A., & Camblong, H. (2012). Sliding-mode control for dfig rotor-and grid-side converters under unbalanced and harmonically distorted grid voltage. *IEEE Transactions on Energy Conversion*, 27(2), 328–339.
- Mechter, A., Kemih, K., & Ghanes, M. (2016). Backstepping control of a wind turbine for low wind speeds. *Nonlinear Dynamics*, 84(4), 2435–2445. <https://doi.org/10.1007/s11071-016-2655-y>.
- Merabet, A., Eshaft, H., & Tanvir, A. A. (2018). Power-current controller based sliding mode control for DFIG-wind energy conversion system. *IET Renewable Power Generation*, 12(10), 1155–1163. <https://doi.org/10.1049/iet-rpg.2017.0313>.
- Mohd Zin, A. A. B., Pesaran, H. A. M., Khairuddin, A. B., Jahanshaloo, L., & Shariati, O. (2013). An overview on doubly fed induction generators' controls and contributions to wind based electricity generation. *Renewable and Sustainable Energy Reviews*, 27, 692–708. <https://doi.org/10.1016/j.rser.2013.07.010>.
- Morawiec, M., Blecharz, K., & Lewicki, A. (2019). Sensorless rotor position estimation of doubly fed induction generator based on backstepping technique. *IEEE Transactions on Industrial Electronics*, 67(7), 5889–5899. <https://doi.org/10.1016/j.jestch.2018.07.005>.
- Mousa, H. H., Youssef, A. R., & Mohamed, E. E. (2019). Variable step size p&o mppt algorithm for optimal power extraction of multi-phase pmsg based wind generation system. *International Journal of Electrical Power & Energy Systems*, 108, 218–231. <https://doi.org/10.1016/j.ijepes.2018.12.044>.
- Naik, K. A., Gupta, C. P., & Fernandez, E. (2020). Design and implementation of interval type-2 fuzzy logic-pi based adaptive controller for dfig based wind energy system. *International Journal of Electrical Power & Energy Systems*, 115, 105468. <https://doi.org/10.1016/j.ijepes.2019.105468>.
- Noussi, K., Abouloifa, A., Katir, H., & Lachkar, I. (2020a). Nonlinear control of active and reactive power in grid-tied dfig-wecs. In *International Conference on Electrical and Information Technologies (ICEIT)*, IEEE (pp 1–6). <https://doi.org/10.1109/ICEIT48248.2020.9113185>.
- Noussi, K., Abouloifa, A., Katir, H., & Lachkar, I. (2019). Modeling and control of a wind turbine based on a doubly fed induction generator. *IEEE*. <https://doi.org/10.1109/ICoCS.2019.8930738>.
- Noussi, K., Abouloifa, A., Katir, H., Lachkar, I., & Giri, F. (2021). Nonlinear control of grid-connected wind energy conversion system without mechanical variables measurements. *IJPEDS*, 12(2), 1139–1149. <https://doi.org/10.11591/ijped.v9.i4.pp1534-1544>.

- Noussi, K., Abouloifa, A., Katir, H., Lachkar, I., Giri, F., & Guerrero, J. (2020b). Nonlinear control of wind energy conversion system based on dfig with a mechanical torque observer. *IFAC-PapersOnLine*, 53(2), 12733–12738. <https://doi.org/10.1016/j.ifacol.2020.12.1890>.
- Patnaik, R., & Dash, P. (2015). Fast adaptive finite-time terminal sliding mode power control for the rotor side converter of the dfig based wind energy conversion system. *Sustainable Energy, Grids and Networks*, 1, 63–84. <https://doi.org/10.1016/j.segan.2015.01.002>.
- Patnaik, R., Dash, P., & Mahapatra, K. (2016). Adaptive terminal sliding mode power control of dfig based wind energy conversion system for stability enhancement. *International Transactions on Electrical Energy Systems*, 26(4), 750–782.
- Rezaei, M. M. (2018). A nonlinear maximum power point tracking technique for dfig-based wind energy conversion systems. *An International Journal of Engineering Science and Technology*, 21(5), 901–908. <https://doi.org/10.1016/j.jestch.2018.07.005>.
- Saad, N. H., Sattar, A. A., & Mansour, A. E. A. M. (2015). Low voltage ride through of doubly-fed induction generator connected to the grid using sliding mode control strategy. *Renewable Energy*, 80, 583–[object Object].
- Şeker, M., Zergeroğlu, E., & Tatlıcioğlu, E. (2016). Non-linear control of variable-speed wind turbines with permanent magnet synchronous generators: a robust backstepping approach. *International Journal of Systems Science*, 47(2), 420–432. <https://doi.org/10.1080/00207721.2013.834087>.
- Sun, D., Wang, X., Nian, H., & Zhu, Z. (2017). A sliding-mode direct power control strategy for dfig under both balanced and unbalanced grid conditions using extended active power. *IEEE Transactions on Power Electronics*, 33(2), 1313–1322. <https://doi.org/10.1109/TPEL.2017.2686980>.
- Xiong, L., Li, P., & Wang, J. (2020). High-order sliding mode control of dfig under unbalanced grid voltage conditions. *International Journal of Electrical Power & Energy Systems*, 117, 105608. <https://doi.org/10.1016/j.epsr.2019.106081>.
- Yang, B., Jiang, L., Wang, L., Yao, W., & Wu, Q. (2016). Nonlinear maximum power point tracking control and modal analysis of dfig based wind turbine. *International Journal of Electrical Power & Energy Systems*, 74, 429–436. <https://doi.org/10.1016/j.ijepes.2015.07.036>.
- Yang, B., Yu, T., Shu, H., Dong, J., & Jiang, L. (2018). Robust sliding-mode control of wind energy conversion systems for optimal power extraction via nonlinear perturbation observers. *Applied Energy*, 210, 711–723. <https://doi.org/10.1016/j.apenergy.2017.08.027>.
- Zamzoum, O., El Mourabit, Y., Errouha, M., Derouich, A., & El Ghzizal, A. (2018). Power control of variable speed wind turbine based on doubly fed induction generator using indirect field-oriented control with fuzzy logic controllers for performance optimization. *Energy Science & Engineering*, 6(5), 408–423. <https://doi.org/10.1002/ese3.215>.

Publisher's Note Springer Nature remains neutral with regard to jurisdictional claims in published maps and institutional affiliations.